


RESEARCH ARTICLE | MARCH 21 2023

Coronavirus peplomer charge heterogeneity ^{EP}

V. Chaurasia ; M. A. Kanso; E. Fried; ... et. al



Physics of Fluids 35, 037125 (2023)

<https://doi.org/10.1063/5.0140851>



CrossMark

Articles You May Be Interested In

Coronavirus peplomer interaction

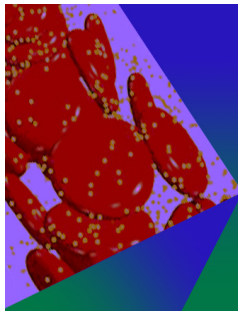
Physics of Fluids (November 2022)

Peplomer bulb shape and coronavirus rotational diffusivity

Physics of Fluids (March 2021)

Coronavirus rotational diffusivity

Physics of Fluids (November 2020)



Physics of Fluids

Special Topic: Flow and Forensics

Submit Today!

Coronavirus peplomer charge heterogeneity

Cite as: Phys. Fluids **35**, 037125 (2023); doi: [10.1063/5.0140851](https://doi.org/10.1063/5.0140851)

Submitted: 31 December 2022 · Accepted: 3 February 2023 ·

Published Online: 21 March 2023



View Online



Export Citation



CrossMark

V. Chaurasia,^{1,a)}  M. A. Kanso,^{1,2}  E. Fried,¹  and A. J. Giacomin^{2,3,4,5} 

AFFILIATIONS

¹Okinawa Institute of Science and Technology, Tancha, Onna, Kunigami District, Okinawa 904-0495, Japan

²Chemical Engineering Department, Polymers Research Group, Queen's University, Kingston, Ontario K7L 3N6, Canada

³Mechanical and Materials Engineering Department, Queen's University, Kingston, Ontario K7L 3N6, Canada

⁴Physics, Engineering Physics and Astronomy Department, Queen's University, Kingston, Ontario K7L 3N6, Canada

⁵Mechanical Engineering Department, University of Nevada, Reno, Nevada 89557-0312, USA

Note: This paper is part of the special topic, Flow and the Virus.

^{a)} Author to whom correspondence should be addressed: vikash.chaurasia2@oist.jp

ABSTRACT

Recent advancements in viral hydrodynamics afford the calculation of the transport properties of particle suspensions from first principles, namely, from the detailed particle shapes. For coronavirus suspensions, for example, the shape can be approximated by beading (i) the spherical capsid and (ii) the radially protruding peplomers. The general rigid bead-rod theory allows us to assign Stokesian hydrodynamics to each bead. Thus, viral hydrodynamics yields the suspension rotational diffusivity, but not without first arriving at a configuration for the cationic peplomers. Prior work considered identical peplomers charged identically. However, a recent pioneering experiment uncovers remarkable peplomer size and charge heterogeneities. In this work, we use energy minimization to arrange the spikes, charged heterogeneously to obtain the coronavirus spike configuration required for its viral hydrodynamics. For this, we use the measured charge heterogeneity. We consider 20 000 randomly generated possibilities for cationic peplomers with formal charges ranging from 30 to 55. We find the configurations from energy minimization of all of these possibilities to be nearly spherically symmetric, all slightly oblate, and we report the corresponding breadth of the dimensionless rotational diffusivity, the transport property around which coronavirus cell attachment revolves.

Published under an exclusive license by AIP Publishing. <https://doi.org/10.1063/5.0140851>

I. INTRODUCTION

As we deepen our understanding of the physical properties of the coronavirus particle, so can we incorporate these new physics into its viral hydrodynamics? Recent advancements in viral hydrodynamics afford the calculation of the transport properties of particle suspensions from first principles, namely, from the detailed particle shapes.^{1–5} For coronavirus suspensions, for example, the shape can be approximated by beading (i) the spherical capsid (Sec. VII of Ref. 1) and then (ii) the radially protruding peplomers (Sec. VII of Refs. 1 and 2). The general rigid bead-rod theory then allows us to proceed by assigning Stokesian hydrodynamics to each bead (Refs. 6 and 7; EXAMPLE 16.7–1 of Ref. 8 or EXAMPLE 13.6–1 of Ref. 9). Table I classifies chronologically prior literature on coronavirus hydrodynamics and defines the novelty of this work. Although our work is motivated mainly by curiosity, its many applications have not escaped our attention. Viral hydrodynamics thus then yields the suspension rotational diffusivity, but not without first arriving at a configuration for the cationic peplomers [see Fig. 1(b) of Ref. 10] Prior work considered identical peplomers, charged identically.^{1–3} However, recent pioneering experiment uncovers

remarkable heterogeneity of both peplomer size [see Fig. 1(a) of Ref. 10; Introduction of Ref. 11] and charge [see Fig. 1(b) of Ref. 10] With permission, we reproduce these seminal results in Fig. 1. By size heterogeneity, we mean that the molecular weights of the peplomer protein trimers vary, and specifically, from Fig. 1, we learn that

$$450 \leq M_p \leq 700. \quad (1)$$

By charge heterogeneity, we mean that the formal charges of the peplomer cations vary, and specifically, from Fig. 1 we learn that

$$30 \leq Q \leq 55, \quad (2)$$

where Q is the integer-valued with mean value $\bar{Q} = 42.29$ electron units. Tables II and III, respectively, define our dimensional and dimensionless symbols. In this paper, exploiting the general rigid bead-rod theory, we carry these pioneering experiments to the implied distribution of rotational diffusivities. The peplomer count on a coronavirus particle, N_p , matters. For the special cases of identical peplomers, charged identically, Fig. 12 of Ref. 1 and Fig. 5 of Ref. 2 give the dimensionless rotational diffusivities for $10 \leq N_p \leq 100$. In this work,

TABLE I. Literature on coronavirus hydrodynamics. Legend: A—with hydrodynamic interactions and Q—cationic charge.

Method	Peplomer population	Hydrodynamic interactions	Capsid shape	Peplomer shape (beads)	Peplomer charge distribution	Reference
Analytical	$10 \leq N_p \leq 100$		Spherical	1	Uniform	1
Analytical	$N_p = 74$		Spherical	3	Uniform	2
Analytical	$N_p = 74$		Ellipsoidal	1	Uniform	3
Molecular dynamics	$N_p = 26$	$A \ll 0.1$	Spherical	1	Uniform	5
Analytical	$N_p = 74$	$0.09 \leq A \leq 0.11$	Spherical	1	Uniform	17
Analytical	$N_p = 74$		Spherical	1	Nonuniform	This work

we use energy minimization^{12,13} for spreading the spikes, charged heterogeneously to obtain the coronavirus spike configuration required for its viral hydrodynamics. For this, we use the measured charge heterogeneity [Fig. 1(b) of Ref. 10]. We consider 20 000 randomly generated possibilities for cationic peplomers with formal charges ranging from 30 to 55. By random generation, we mean that we randomize the formal charge of each of the $N_p = 74$ peplomers over the measured range. We rely on our previous literature review (see Table X of Ref. 1) to choose $N_p = 74$. Calculations of the rotational diffusivity of coronavirus suspensions initially excluded interferences of Stokes flow velocity fields between nearby peplomers.^{1–3} More recently, the method for incorporating hydrodynamic interactions was advanced (Sec. III of Ref. 15) and used (Sec. V of Refs. 15 and 16) and even applied to coronavirus suspensions.¹⁷ However, in this work, we neglect hydrodynamic interactions for formal charge distribution of coronavirus peplomer protein trimers, leaving this detail for another day. Our work here is about the heterogeneity of formal charge from one peplomer to another, which is separate from the local charge distribution over the surface of an individual peplomeric cation, which has been simulated (see Fig. 2 of Ref. 18) but not measured. These beautiful distributions are averaged over many peplomers and are thus silent on peplomer-to-peplomer heterogeneity. The heterogeneity of this local charge distribution is yet to be discovered. Our formulation of

the general rigid bead-rod theory is limited to axisymmetric viruses. By axisymmetry, we mean that both the virus particle and its moment of inertia ellipsoid have at least one axis of symmetry (Refs. 19 and 20, Chap. 13 of Ref. 9, and Chap. 16 of Ref. 8). Furthermore, if the virus particle structure is axisymmetric, at least two of its principal moments of inertia equate at any angle from the molecular axis. Since the coronavirus particle structure is axisymmetric, so will its moment of inertia ellipsoid. Our usage of axisymmetric is not to be confused with the common geometric meaning of continuous rotational symmetry about an axis. In the tradition of the transport sciences, we define the rotatory diffusivity as (see Footnote 2 of p. 62 of Ref. 8)

$$D_{\text{rot}} \equiv \frac{2kT}{\zeta}, \quad (3)$$

which, for any axisymmetric macromolecule, from the general rigid bead-rod theory, gives

$$D_{\text{rot}} \equiv \frac{12L^2}{\nu D_r}, \quad (4)$$

which has the dimensions of diffusivity and is four times the translational diffusivity

$$D_{\text{rot}} \equiv 4D_{tr} \quad (5)$$

or

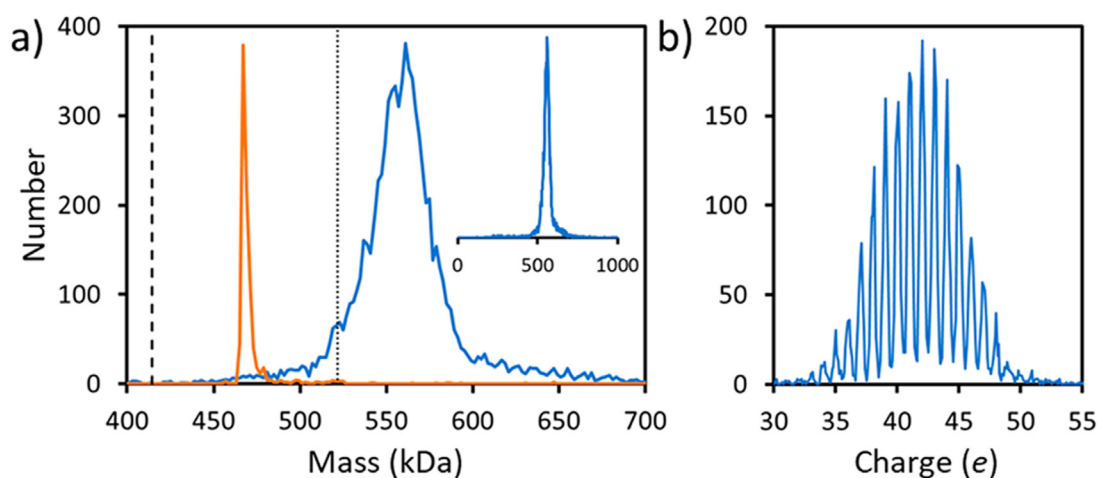

FIG. 1. Measured size [panel (a)] and charge [panel (b)] heterogeneities of coronavirus peplomer protein trimers (blue curves). Reprinted with permission from Fig. 1 of Miller *et al.*, *J. Am. Chem. Soc.* **143**(10), 3959–3966 (2021). Copyright 2021 American Chemical Society.

TABLE II. Dimensional variables. Legend: M —mass, L —length, and t —time.

Name	Unit	Symbol
Angular frequency	t^{-1}	ω
Augmented energy functional	ML^2/t^2	\hat{E}
Bead friction coefficient	M/t	ζ
Complex viscosity	M/Lt	η^*
Dielectric permittivity	T^4I^2/ML^3	ϵ
Element for Kronecker delta	t^{-1}	$\delta(s)$
Kinetic molecular energy per molecule	ML^2/t^2	kT
Length of the spike of each peplomer	L	ℓ
Mass	M	m
Mean value of charge distribution	e	\bar{Q}
Minus the imaginary part of the complex viscosity	M/Lt	η''
Molecular weights of the peplomer protein trimers	M/mol	M_p
Nearest bead center-to-center distance	L	L
Number of dumbbells per unit volume	$1/L$	n
Point charge	e	Q
Real part of the complex viscosity	M/Lt	η'
Relaxation modulus	M/L	$G(s)$
Relaxation time of rigid dumbbell	t	λ_0
Relaxation time of solution	t	λ
Rotational diffusivity	t^{-1}	D_r
Rotatory diffusivity	L^2/t	D_{rot}
Shear rate amplitude	t^{-1}	$\dot{\gamma}^0$
Solvent viscosity	M/Lt	η_s
Time difference	t	$s \equiv t - t'$
Total electrostatic energy	ML^2/t^2	E
Translational diffusivity	L^2/t	D_{tr}
Viscosity, zero-shear	M/Lt	η_0
Zero-shear first normal stress difference	M/L	$\psi_{1,0}$

$$D_r = \frac{\nu}{3L^2} D_{tr}. \tag{6}$$

In this paper, we depart from the said transport tradition of using the rotatory diffusivity, D_{rot} , and frame our results in terms of the rotational diffusivities, D_r , of coronavirus particles.

TABLE IV. Parameters of the normal distribution of different quantities.

Quantity x	Equation	Figure	Parameters of the normal distribution $f = Ae^{-(x-\mu)^2/2\sigma^2}$		
			A	μ	σ
Q	Eq. (2)	Fig. 3	0.1153	41.586	3.5251
$\log(F - \min F)$	Eq. (31)	Fig. 5(b)	0.6082	-6.3755	0.6423
I_1		Fig. 7	3.0800	158.22	0.1310
I_2			3.9447	158.56	0.1007
I_3			3.0926	158.91	0.1304
λ/λ_0	Eq. (11)	Fig. 11	1.5296	3.1644	0.2669
$\lambda_0 D_r$	Eq. (16)	Fig. 12	9.1324×10^5	5.2670×10^{-4}	4.4882×10^{-7}

TABLE III. Dimensionless variables and groups.

Name	Symbol
Amplitude, mean value, and variance of normal distribution	A, μ, σ^2
Aspect ratio	c/a
Capsid-sphere	\mathcal{C}
Coefficient in Eqs. (19) and (20)	a
Coefficient in Eqs. (19) and (20)	b
Coefficient in Eqs. (19) and (20)	ν
Augmented Lagrangian	\hat{E}
Charge	q_i
Electrostatic energy	\bar{E}
Wales's electrostatic energy	E_w
Electrostatic energy relative to Wales's energy	F
Deborah number, oscillatory shear	$D_e \equiv \lambda\omega$
Principal moment of inertia	I_1, I_2, I_3
Normal distribution	f
Probability distribution function	pdf
Sphere on which peplomers lie	\mathcal{S}
Total number of beads	N
Total number of peplomers	N_p
Weissenberg number	$Wi \equiv \lambda\dot{\gamma}^0$

II. METHOD

In the general rigid bead-rod theory, we construct macromolecules from sets of beads whose positions, relative to one another, are fixed. The macromolecular bead-rod models of our coronavirus particles are suspended in a Newtonian solvent. In this work, we neglect interactions of the solvent velocity fields, be they between nearest beads^{21,22} or nearest macromolecules. With the general rigid bead-rod theory, we thus locate beads to sculpt an approximation of the coronavirus particle shapes. In this way, using the general rigid bead-rod theory, we can model any virus macromolecular architecture (see Fig. 9 of Ref. 7). For the general rigid bead-rod theory, Hassager arrived at general equation of the shear relaxation function [Eq. (48) of Ref. 19]:

$$\frac{G(s)}{nkT} = \frac{\delta(s)}{kT} \left(\frac{2\eta_s}{n} + \zeta L^2 a \right) + be^{-s/\lambda} \tag{7}$$

with

$$a \equiv \frac{10I_1 + 5I_3 - 6(I_1 - I_3)^2}{30}, \tag{8}$$

$$b \equiv \frac{3}{5} \left(1 - \frac{I_3}{I_1} \right)^2, \tag{9}$$

$$\nu \equiv \frac{6}{I_1}, \tag{10}$$

and

$$\frac{\lambda}{\lambda_0} = 2I_1 = \frac{12}{\nu}, \tag{11}$$

where $I_1, I_2,$ and I_3 are the dimensionless principal moment of inertia (see Tables III and IV of Ref. 23). For axisymmetric macromolecules, $I_1 = I_2$. And the respective definitions for oblate and prolate for such molecules are

$$I_3 \geq I_1 \tag{12}$$

and

$$I_3 \leq I_1, \tag{13}$$

which we will use below. From the general rigid bead-rod theory (Figs. 3 and 17 of Refs. 7 and 24), we learn that all axisymmetric macromolecules lie on either the upper (oblate) or lower (prolate) branches of the $(a\nu, b)$ plane [Eqs. (23) and (22) of Ref. 7, respectively, from Eq. (21) of Ref. 7]

$$a^2b^2 + \frac{2(b-9)a\nu}{3} + \frac{b^2 - 33b + 81}{9} = 0. \tag{14}$$

We use Eqs. (3)–(13) in Ref. 7 to compute the rotational diffusivity (see Footnote 2 of p. 62 of Ref. 8):

$$D_r \equiv \frac{1}{6\lambda} \tag{15}$$

or [Eq. (23) of Ref. 1]:

$$\lambda_0 D_r = \frac{\nu}{72}, \tag{16}$$

which we will use to arrive at our results below.

III. OSCILLATORY SHEAR FLOW

In this paper, we focus on small-amplitude oscillatory shear flow (SAOS). For this flow field, for the molecular definition of small amplitude, the general rigid bead-rod theory yields [Eq. (32) of Ref. 7]

$$\lambda \dot{\gamma}^0 \ll \frac{1}{\nu\sqrt{2}}, \tag{17}$$

whose left side is the macromolecular Weissenberg number. The polymer contributions to the complex viscosity^{25,26}

$$\eta^* \equiv \eta' - i\eta'' \tag{18}$$

are [Eqs. (40) and (41) of Ref. 7]

$$\frac{\eta' - \eta_s}{\eta - \eta_s} = \left(\frac{a\nu}{2b} + 1 \right)^{-1} \left(\frac{a\nu}{2b} + \frac{1}{1 + (\lambda\omega)^2} \right) \tag{19}$$

and

$$\frac{\eta''}{\eta - \eta_s} = \left(\frac{a\nu}{2b} + 1 \right)^{-1} \frac{1}{1 + (\lambda\omega)^2}, \tag{20}$$

where $\lambda\omega$ is the Deborah number. Equations (19) and (20) each capture non-Newtonian behavior: (i) Eq. (19) captures the descent of $\eta'(\omega)$ and (ii) Eq. (20) captures the ascent of $\eta''(\omega)$ from the origin. In this paper, we plot the real and minus the imaginary parts of the shear stress responses to small-amplitude oscillatory shear flow as functions of frequency, following Ferry (Secs. 2.A.4.–2.A.6. of Ref. 27) or Bird *et al.* (Sec. 4.4 of Ref. 28) As $\omega \rightarrow 0$, for the polymer contribution to the zero-shear viscosity, we get

$$\frac{\eta_0 - \eta_s}{nkT\lambda} = \frac{a\nu}{2} + b = b \left(\frac{a\nu}{2b} + 1 \right) \tag{21}$$

and for the zero-shear first normal stress difference coefficient

$$\frac{\psi_{1,0}}{\lambda(\eta_0 - \eta_s)} = 2 \left(\frac{a\nu}{2b} + 1 \right)^{-1}. \tag{22}$$

For future reference, we denote a normal distribution of a quantity x by

$$f = Ae^{-\frac{(x-\mu)^2}{2\sigma^2}}, \tag{23}$$

where $A, \mu,$ and σ^2 are, respectively, the amplitude, mean value, and variance of x .

IV. PEPLIMER CONFIGURATIONAL HETEROGENEITY

A. Kinematics

Let N_p be the number of peplomers attached to the capsid-sphere \mathcal{C} of radius r_c . Let ℓ be the length of the spike of each peplomer attached normal to \mathcal{C} at the point of contact on \mathcal{C} . Therefore, each peplomer must lie on a sphere \mathcal{S} of radius $r_s = r_c + \ell$, as shown in Fig. 2. Denoting the position vector of i th bead by $r_s \mathbf{r}_i$, the dimensionless position vector \mathbf{r}_i must obey N_p scalar equations

$$|\mathbf{r}_i|^2 = 1, \quad i = 1, \dots, N_p \tag{24}$$

so that in a dimensionless setting, the peplomer bead centers lie on a sphere of unit radius.

B. Energetics

Let $\bar{Q}q_i$ be the charge on i th bead, where $\bar{Q} = 42.29$ electron unit is the mean value of the experimentally measured heterogeneous distribution of the charges on the peplomers by Miler *et al.*,¹⁴ as shown in Figs. 1(b) and 3. Interestingly, the charge distribution follows a normal distribution, parameters of which are provided in Table IV. Here, q_i denotes the dimensionless charge on i th peplomer. The total electrostatic energy of such N_p peplomers, constrained to a sphere \mathcal{S} of radius r_s , is given by

$$E = \frac{\bar{Q}^2}{4\pi\epsilon r_s} \sum_{i=1}^{N_p} \sum_{j<i}^{N_p} \frac{q_i q_j}{|\mathbf{r}_i - \mathbf{r}_j|}, \tag{25}$$

where ϵ is the dielectric permittivity. We use the quantity

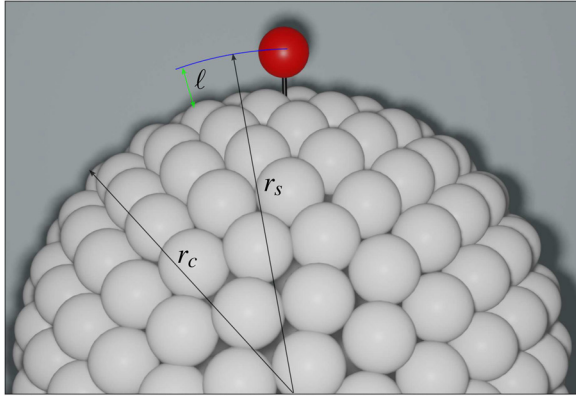


FIG. 2. Coronavirus capsid sphere \mathcal{C} of radius r_c beaded with gray spheres and a peplomer represented with red bead and black stick of length ℓ attached to \mathcal{C} are shown. The peplomer bead lies on a sphere \mathcal{S} of radius $r_s = r_c + \ell$. While considering electrostatic interaction, we assume that the white spheres are chargeless and a peplomer is endowed with a point charge, concentrated to the center of the red sphere.

$$\frac{\bar{Q}^2}{4\pi\epsilon r_s}, \tag{26}$$

which is the electrostatic energy between two point charges with charge \bar{Q} and r_s distance apart, as the energy scale, and define the dimensionless total electrostatic energy of N_p peplomers by

$$\tilde{E} = \frac{4\pi\epsilon r_s E}{\bar{Q}^2} = \sum_{i=1}^{N_p} \sum_{j=1}^{j<i} \frac{q_i q_j}{|\mathbf{r}_i - \mathbf{r}_j|}, \tag{27}$$

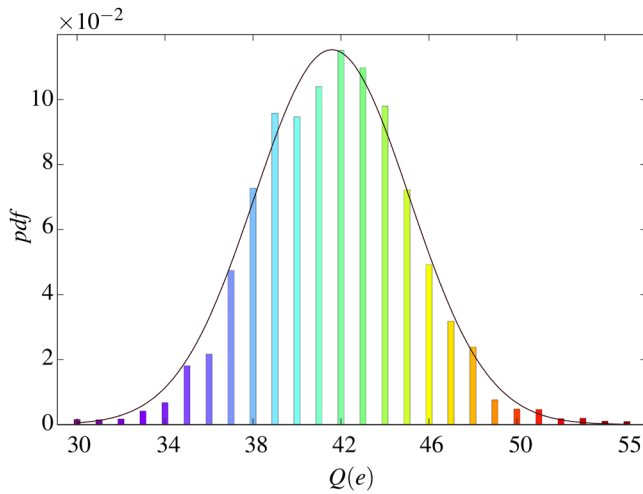


FIG. 3. Probability distribution function *pdf* of coronavirus peplomer protein trimers for which $30 \leq Q \leq 55$, abstracted from measurements of Fig. 1(b). Probability-charge colors in spectral order, with the highest probability formal charge of $Q = 42$ in green, with red–orange–yellow for $30 \leq Q < 42$, and blue–indigo–violet for $42 < Q \leq 55$. Data fit well with a normal distribution f , as shown with the solid black curve. See Eq. (23) and Table IV for the definition and parameters of f .

where $\mathbf{r}_i, i = 1, \dots, N_p$ are the dimensionless position vectors of the peplomers bead centers. We will use Eq. (27) in Sec. IV C to determine configurations minimizing the dimensionless electrostatic energy \tilde{E} .

C. Equilibrium equations

We have assumed that beads are endowed with strictly positive charges $\bar{Q}q_i, i = 1, \dots, N_p$. Therefore, the beads repel each other and would prefer to distribute themselves as far as possible from each other to minimize the dimensionless electrostatic energy \tilde{E} , defined in Eq. (27). Using a constrained minimization approach, we find an equilibrium distribution that locally minimizes the energy in Eq. (27) while satisfying kinematic constraint in Eq. (24), for given dimensionless charges $q_i, i = 1, \dots, N_p$ and number N_p of peplomers. The following are the details of the constrained minimization approach. We define the augmented energy functional by

$$\hat{E} = \sum_{i=1}^{N_p} \left(\sum_{j=1}^{j<i} \frac{q_i q_j}{|\mathbf{r}_i - \mathbf{r}_j|} - \rho_i |\mathbf{r}_i|^2 \right), \tag{28}$$

where $\rho_i, i = 1, \dots, N_p$, are the dimensionless Lagrange multipliers required to enforce the kinematic constraints in Eq. (24). We obtain the Euler–Lagrange equations by differentiating Eq. (28) with the dimensionless position vectors $\mathbf{r}_i, i = 1, \dots, N_p$, and equating the resulting expressions to $\mathbf{0}$,

$$-q_i \sum_{j=1, j \neq i}^{N_p} \frac{q_j (\mathbf{r}_i - \mathbf{r}_j)}{2|\mathbf{r}_i - \mathbf{r}_j|^3} - \rho_i \mathbf{r}_i = \mathbf{0}, \quad i = 1, \dots, N_p. \tag{29}$$

In the Euler–Lagrange equation [Eq. (29)], the first term on the left-hand side is the total dimensionless electrostatic force exerted on the i th bead by all the remaining beads. For an equilibrium, this electrostatic force is balanced by the second term in Eq. (29), $-\rho_i \mathbf{r}_i$, which is the dimensionless reactive force between the capsid and i th bead required to satisfy Eq. (24), that is, to maintain contact of that bead with the capsid. Therefore, the term $-\rho_i \mathbf{r}_i, i = 1, \dots, N_p$, in Eq. (29) is a measure of the interaction between the capsid and i the bead. Notably, if all the peplomer beads are positively charged, they will repel each other. Therefore, for equilibrium, the electrostatic interaction between the peplomer beads and the capsid must be attractive to counter the repulsive forces between the beads. In this respect, we follow Refs. 12 and 29, wherein a Lagrange multiplier is used to represent the adhesive reaction between a semiflexible polymer and a rigid spherical substrate.³⁰ as well used Lagrange multipliers to describe the adhesive reaction between a generalized surface and confined semiflexible polymers. Another example of this approach appears in the work of Ref. 31, who introduced a Lagrange multiplier to predict adhesive reactions.

For each value of i in the vector equation [Eq. (29)], there are three scalar equations. Thus, Eq. (29) yields $3N_p$ scalar equations. We solve a total of $4N_p$ equations, $3N_p$ equilibrium equations in Eq. (29), and N_p constraints in Eq. (24), simultaneously to determine $4N_p$ unknowns, $3N_p$ scalar components of N_p position vectors in \mathbf{r}_i , and N_p in scalar Lagrange multipliers $\rho_i, i = 1, 2, \dots, N_p$. We use the *Levenberg–Marquardt* Algorithm from the *fsolve* package of MATLAB to solve the system of equations with 10^{-16} error tolerance to

determine the energy minimizing configuration for given values of $\bar{Q}q_i$, $i = 1, \dots, N_p$ charges.

Our model, which has a spherical core, amounts to a modified version of the Thompson problem,³² wherein one seeks to find a state that distributes N_p electrons over a unit sphere as evenly as possible, with minimum electrostatic energy. Wales *et al.*^{33,34} solved this problem for identically charged particles by minimizing the dimensionless energy functional

$$E_w = \sum_{i=1}^{N_p} \sum_{j=1}^{j<i} \frac{1}{|\mathbf{r}_i - \mathbf{r}_j|} \quad (30)$$

providing solutions for a large set of values of N_p , where \mathbf{r}_i , $i = 1, \dots, N_p$, are the dimensionless position vectors of unit point charges on a unit sphere. By contrast, our energy minimization solves the problem for particles not charged identically (i th peplomer has q_i dimensionless charge). Our energy expression [Eq. (27)] recovers the energy expression [Eq. (30)] of Wales *et al.*^{33,34} for $q_i = 1$, $i = 1, \dots, N_p$, and thus, we recover the Thompson solution (energy minimization over a spherical surface about which much has been written¹⁰) as it should (see Sec. VII of Ref. 7) As far as we know, we are the first to perform an energy minimization of heterogeneously charged particles over the surface of a sphere.

To investigate the effect of heterogeneous charge distribution on the total electrostatic energy relative to identically charged beads studied by Wales *et al.*,^{33,34} we define a dimensionless electrostatic energy

$$F = \frac{E}{E_w} - 1 = \sum_{i=1}^{N_p} \sum_{j=1}^{j<i} \frac{q_i q_j}{E_w |\mathbf{r}_i - \mathbf{r}_j|} - 1, \quad (31)$$

where \bar{E} and E_w are defined in Eqs. (27) and (30), respectively. In this work, we restrict our attention to $N_p = 74$, for which Wales *et al.*^{33,34} calculated $E_w = 2387.07$.

V. RESULTS

Since Q is integer-valued, we next abstract from Fig. 1 the formal charge distribution line spectrum of coronavirus peplomer protein trimers. We give this in Fig. 3, from which we glean Eq. (2), as we must. Whereas Fig. 3 and its companion [Eq. (2)] tell us the charge heterogeneity, these are silent on how these peplomer charges will arrange themselves over the coronavirus surface. In this work, we examine 20 000 possible arrangements of number $N_p = 74$ of peplomers, which we call states. For a given state, we randomly draw $\bar{Q}q_i$, $i = 1, \dots, N_p$, charges from the discrete, integer-valued bin of charges in the interval $30 \leq Q \leq 55$ with probability as per experimental measurement,¹⁴ as shown in Fig. 3. Next, we follow the energy minimization method of Sec. IV C to determine the minimum energy configuration of that state. We repeat the process of randomly drawing $\bar{Q}q_i$, $i = 1, \dots, N_p$, charges from the discrete, integer-valued bin 20 000 times and determine the energy minimizing configuration of each state. Figure 4 illustrates one such energy-minimized state, with color coding for the formal charges. Although considering a larger number of states than 20 000 will give us a more comprehensive understanding of the effect of charge heterogeneity, we restrict our attention to 20 000 states due to computational cost limitations. We expect that the practically chosen number of states is large enough to derive meaningful conclusions.

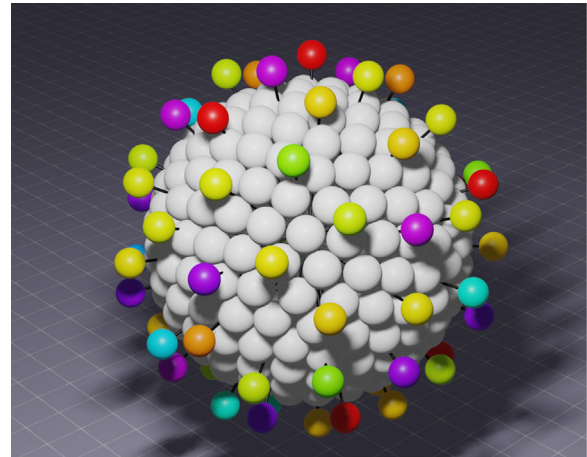


FIG. 4. Minimum energy configuration of one charge state of a coronavirus particle of $N_p = 74$ and $N_c = 256$. Bead colors in spectral order, with the highest probability formal charge of $Q = 42$ in green, with red–orange–yellow for $30 \leq Q < 42$, and blue–indigo–violet for $42 < Q \leq 55$. The peplomer rods do not generally align with the bead centers of the beaded capsid.

Dimensionless electrostatic energy F , defined in Eq. (31), of the 20 000 reasonable states is provided in Fig. 5(a). The red horizontal line in the figure corresponds to $F = 0$ at which, using Eq. (31), the dimensionless electrostatic energy \bar{E} , defined in Eq. (27), of our heterogeneously charged system is equal to the dimensionless electrostatic energy E_w , defined in (30) of an identically charged system with unit charge for $N_p = 74$. We find 687 states with $E < E_w$. Moreover, we find that the energy of states shown in Fig. 5(a) follows a log–normal distribution, as shown in the histogram in Fig. 5(b). Sorting on these minimum energies, E , we construct Fig. 6, which inflect at about the 10 000 state. The lowest value of F (vertical intercept of Fig. 6), defined in Eq. (31), is $F = -4.2625 \times 10^{-4}$. We next calculate the dimensionless moments of inertia tensor of each state, from which we calculate the dimensionless principal moment of inertia I_1 , I_2 , and I_3 . We arrange those quantities into the three histograms of Fig. 7, from which we learn that

$$157.63 \leq I_1 \leq I_2 \leq I_3 \leq 159.44, \quad (32)$$

and thus, $I_1 \approx I_2 \approx I_3$. That is, every state is nearly axisymmetric. Figure 8 maps all of the energy-minimized arrangements onto $(av - 3, b)$ plane. For a spherical geometry, $av = 3$ and for oblate and prolate geometries, respectively, $av > 3$ and $av < 3$. Since in Fig. 8, $av > 3$, all of our 20 000 heterogeneously charged coronavirus states are slightly oblate. Figures 9 and 10 illustrate the diversity of rheological behaviors among our 20 000 coronavirus states. From Fig. 9, we learn that the highest energy states give the most significant departures from Newtonian behavior for the real part of the complex viscosity

$$\frac{\eta' - \eta_s}{\eta_0 - \eta_s} < 1. \quad (33)$$

Likewise, from Fig. 10, we learn that the highest energy states give the largest departures from Newtonian behavior for minus the imaginary part of the complex viscosity:

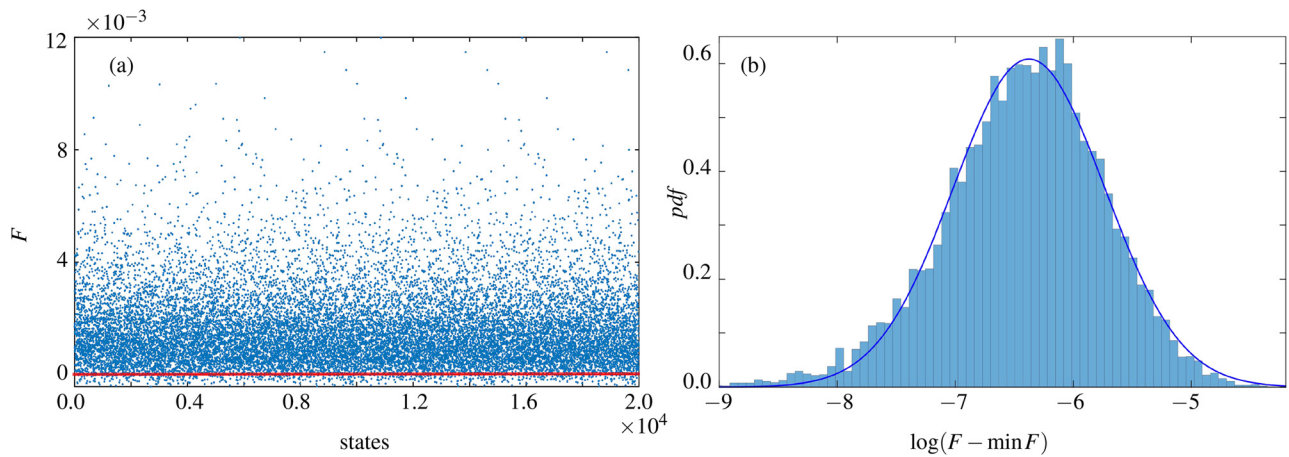


FIG. 5. (a) Dimensionless electrostatic energy F , defined in (31), of 20 000 equilibrium states. The red line shows the energy level for uniform charge distribution. We find 687 equilibrium states with energy lower than that level. (b) Probability distribution function pdf vs $\log(F - \min F)$ of the states shown in (a). Data fit well with a normal distribution f , defined in (31), shown with the blue curve. See Table IV for parameters of f .

$$\frac{\eta''}{\eta_0 - \eta_s} > 1. \tag{34}$$

We next use Eq. (11) to arrive at the heterogeneity of the relaxation times following on from the pioneering charge heterogeneity experiments of panel b) of Fig. 1 to get Fig. 11. From this figure, we learn that the measured formal charge distribution of Eq. (2), through the lens of the general rigid bead-rod theory, implies that the coronavirus relaxation time varies in the interval

$$315.26 \leq \frac{\lambda}{\lambda_0} \leq 317.04. \tag{35}$$

Using Eq. (16), we next construct Fig. 12. From this figure, we learn that the measured formal charge distribution of Eq. (2), through the lens of the general rigid bead-rod theory, implies the coronavirus dimensionless rotational diffusivity distribution of

$$5.257 \times 10^{-4} \leq \lambda_0 D_r \leq 5.287 \times 10^{-4}. \tag{36}$$

Equations (35) and (36) are the main results of this work. Recall that the rotational diffusivity is the transport property around which coronavirus cell attachment revolves. From Eq. (36), we learn that through its heterogeneity of peplomer formal charges [Eq. (2)], even if all capsids are spherical, and all of these with $N_p = 74$, the coronavirus attacks with a distribution of rotational diffusivities. We find Fig. 12 to be intrinsically beautiful.

VI. CONCLUSION

We began this paper by distinguishing two forms of higher energy coronavirus peplomer arrangement arising for fixed peplomer population: (i) those caused by the heterogeneity of charge from one peplomer to the next and (ii) those caused by local energy minima at a uniform

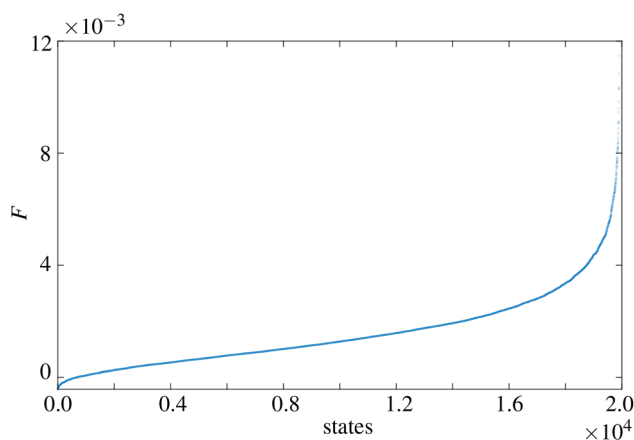


FIG. 6. Sorted dimensionless electrostatic energy F , defined in (31), of 20 000 states for formal charge distribution of coronavirus peplomer protein trimers of Fig. 3 ($N_p = 74$).

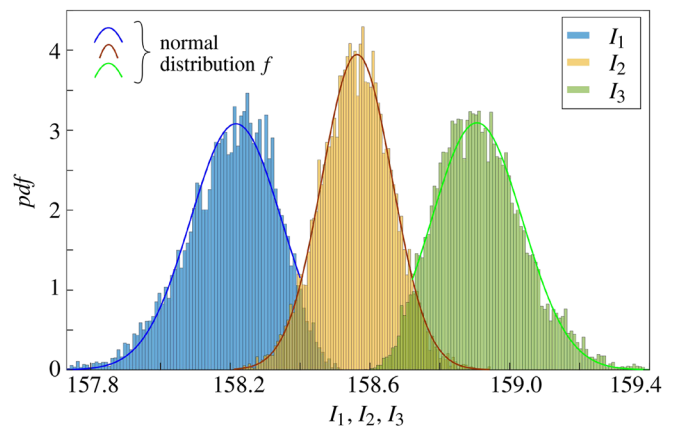


FIG. 7. Probability distribution function pdf of the dimensionless principal moment of inertia I_1 , I_2 , and I_3 of 20 000 equilibrium states. We find that $157.63 \leq I_1 \leq I_2 \leq I_3 \leq 159.44$, and thus, every state is nearly axisymmetric. Normal distribution f , defined in Eq. (23), fits well for each of those quantities, as shown with blue, brown, and green colors. See Table IV for parameters of f .

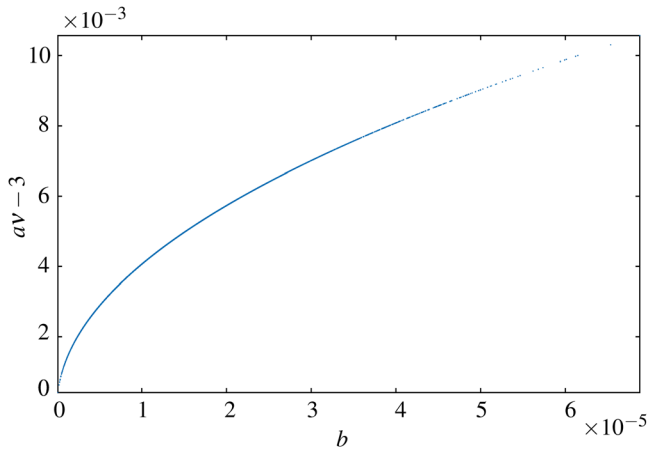


FIG. 8. Configurations for formal charge distribution of coronavirus peplomer protein trimers of Fig. 3 mapped onto $(a\nu - 3, b)$ plane for number $N_p = 74$ of peplomers using Eqs. (8)–(10). Since $a\nu > 3$, all states are oblates.

charge (less probable than the lowest energy configuration^{33,34}). In this paper, we focused on the former romanette because this charge heterogeneity has been recently observed and quantified experimentally (Fig. 1. of Ref. 14 reprinted as Fig. 1). For the romanette (i), we have examined the lowest energy (and thus the most probable) configuration for each of 20 000 random charge arrangements (see one of these in Fig. 4). By contrast, romanette (ii) would involve examining lower probability arrangements (higher energy and local energy minima) arising for any fixed charge arrangement (be it with or without^{33,34} charge heterogeneity). Romanettes (i) and (ii) yield multiplicities of relaxation time, thus multiplicities of coronavirus transport properties. We leave the intriguing problem of the relaxation time distribution implied by romanette (ii) for another day. In this paper, we calculate the transport properties of coronavirus suspensions from the first principles, namely, from the detailed particle shapes. For this, we approximated the shape by beading (i) the spherical capsid and then (ii) the radially protruding peplomers (see

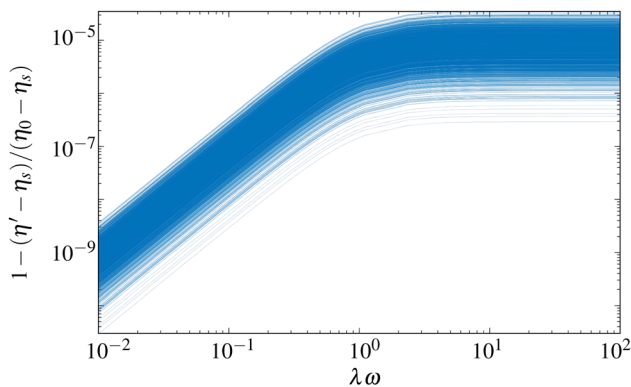


FIG. 9. Log–log plot of the shifted real part of the complex viscosity function using Eq. (19) for each configuration from the formal charge distribution of coronavirus peplomer protein trimers of Fig. 3 with $N_p = 74$. The bottom curve is the lowest energy (global minimum), with 20 000 higher energy states falling successively above this bottom curve.

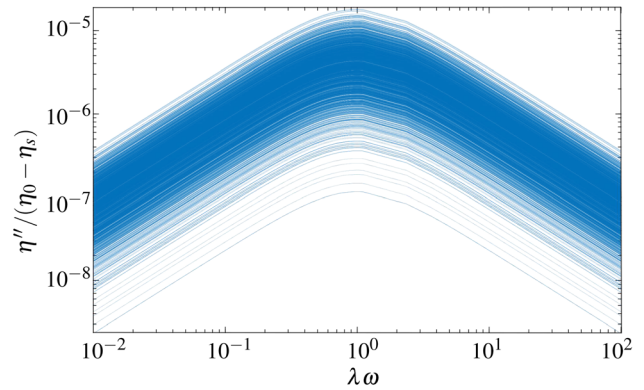


FIG. 10. Log–log plot of minus the imaginary part of the complex viscosity function using Eq. (20) for each configuration from the formal charge distribution of coronavirus peplomer protein trimers of Fig. 3 with $N_p = 74$. The bottom curve is the lowest energy (global minimum), with 20 000 higher energy states stacking successively above this bottom curve.

gray and colored beads of Fig. 4, respectively). Following the general rigid bead-rod theory, we assigned Stokesian hydrodynamics to each bead position. Our work, called viral hydrodynamics, thus then yields the suspension rotational diffusivity equation [Eq. (36)], but not without first arriving at a configuration for the cationic peplomers. From the general rigid bead-rod theory, we learn that the transport properties depend upon the macromolecular moments of inertia. By transport properties, we mean the rotational diffusivity, the relaxation time [Eq. (11)] upon which the rotational diffusivity depends, and the complex viscosity equations [Eqs. (18)–(20)]. In this work, we considered 20 000 randomly generated possibilities for cationic peplomer arrangements with formal charges ranging from 30 to 55 [Eq. (2)]. We find the configurations from energy minimization of all of these possibilities to be nearly spherically symmetric (Figs. 7 and 8), all slightly oblate, and we report the corresponding

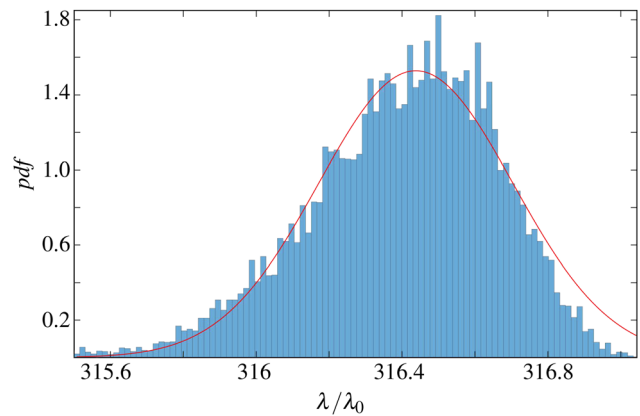


FIG. 11. Probability distribution function *pdf* of Coronavirus dimensionless relaxation time using Eq. (11) ($315.26 \leq \lambda/\lambda_0 \leq 317.04$) for heterogeneously charged peplomer population of $N_p = 74$ with formal charge range $30 \leq Q \leq 55$ abstracted from the formal charge distribution of coronavirus peplomer protein trimers of Fig. 3 (20 000 states). Solid curve denotes a normal distribution fit *f*. See Eq. (23) and Table IV for the definition and parameters of *f*.

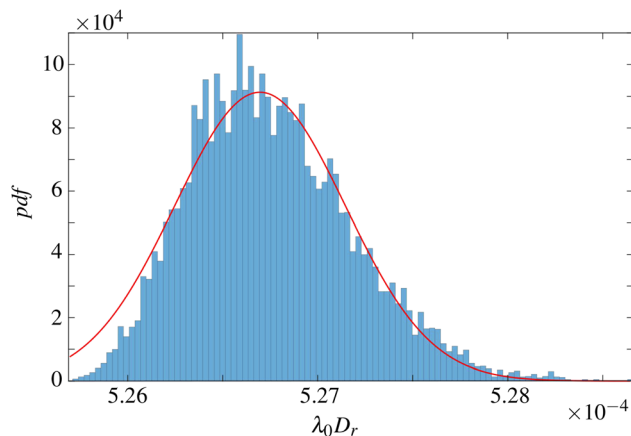


FIG. 12. Probability distribution function pdf of coronavirus dimensionless rotational diffusivity using Eq. (16). Due to heterogeneously charged peplomer population of $N_p = 74$ with formal charge range $30 \leq Q \leq 55$ abstracted from the formal charge distribution of coronavirus peplomer protein trimers of Fig. 3 (20 000 states), the rotational diffusivity varies in the interval $5.257 \times 10^{-4} \leq \lambda_0 D_r \leq 5.287 \times 10^{-4}$. The solid red curve denotes a normal distribution fit f . See Eq. (23) and Table IV for the definition and parameters of f .

breadth of the dimensionless relaxation time distribution in Fig. 11 and Eq. (35) and rotational diffusivity in Fig. 12 and Eq. (36), the transport property around which coronavirus cell attachment revolves. In this paper, exploiting the general rigid bead-rod theory, we carried the pioneering experiments on peplomer formal charge heterogeneity through to what this implies about the rotational diffusivity, and specifically about its heterogeneity. From Fig. 12 and Eq. (36), we learn that the coronavirus attacks with a distribution of rotational diffusivities. In this paper, we have neglected the interferences of velocity profiles of nearby peplomers.¹⁷ We call these interferences hydrodynamic interactions. We leave the exploration of how formal charge distribution of coronavirus peplomer protein trimers is affected by hydrodynamic interactions for future work. We would account for such hydrodynamic interactions following the method of Sec. II of Ref. 10 with $A \equiv L/2d \approx 1/10$ [Eq. (8) of Ref. 10]. Our work is silent about the charge distribution over the surfaces of individual peplomers, recently quantified by molecular dynamics simulation (see Fig. 2. of Ref. 18). We leave this intriguing task for the future. Docking coronavirus with a receptor site requires not just one but two adjacent peplomers to align and attach. For this probability, see Eq. (1) of Ref. 1. This has yet to be calculated for peplomers charged identically, and our work is silent on how this probability would be affected by the recently measured peplomer formal charge heterogeneity. We leave this daunting task for another day.

ACKNOWLEDGMENTS

This research was undertaken, in part, thanks to support from the Canada Research Chairs program of the Government of Canada for the Natural Sciences and Engineering Research Council of Canada (NSERC) Tier 1 Canada Research Chairs in Rheology, and in *Physics of Fluids*. This research was also undertaken, in part, thanks to support from the Discovery Grant program of the

Natural Sciences and Engineering Research Council of Canada (NSERC) (A. J. Giacomin), Vanier Canada Graduate Scholarship (M. A. Kanso), and the Mitacs Research Training Award (A. J. Giacomin and M. A. Kanso). V. Chaurasia and E. Fried gratefully acknowledge support from the Okinawa Institute of Science and Technology Graduate University with subsidy funding from the Cabinet Office, Government of Japan. We are grateful to the anonymous referees for helping us improve the manuscript.

AUTHOR DECLARATIONS

Conflict of Interest

The authors have no conflicts to disclose.

Author Contributions

Vikash Chaurasia: Conceptualization (equal); Data curation (lead); Formal analysis (lead); Resources (equal); Software (lead); Validation (lead); Visualization (lead); Writing – original draft (equal); Writing – review & editing (equal). **Mona Kanso:** Project administration (lead); Writing – original draft (equal). **Eliot Fried:** Conceptualization (equal); Funding acquisition (equal); Supervision (equal). **Alan Jeffrey Giacomin:** Conceptualization (lead); Funding acquisition (equal); Investigation (equal); Methodology (equal); Resources (equal); Supervision (lead); Validation (equal); Writing – original draft (lead); Writing – review & editing (equal).

DATA AVAILABILITY

The data that support the findings of this study are available from the corresponding author upon reasonable request.

REFERENCES

- M. A. Kanso, J. H. Piette, J. A. Hanna, and A. J. Giacomin, “Coronavirus rotational diffusivity,” *Phys. Fluids* **32**(11), 113101 (2020); Feature article, cover article.
- M. A. Kanso, V. Chaurasia, E. Fried, and A. J. Giacomin, “Peplomer bulb shape and coronavirus rotational diffusivity,” *Phys. Fluids* **33**(3), 033115 (2021); Part 2, Editor’s Pick.
- M. A. Kanso, M. Naime, V. Chaurasia, K. Tontiwattanakul, E. Fried, and A. J. Giacomin, “Coronavirus pleomorphism,” *Phys. Fluids* **34**(6), 063101 (2022); Part 1, Feature article, Scilight. Errata: In Table III, rows 1–4 of columns 2–5 and 10 should be divided by k , and of columns 7 and 11, by k^{-1} , where $k = 52^2$. In FIG. 11, the ordinate should be divided by k^{-1} . In Fig. 7, the ordinate and abscissa should be divided by k .
- M. A. Kanso, “Coronavirus hydrodynamics,” Ph.D. thesis (Polymers Research Group, Chemical Engineering Department, Queen’s University, Kingston, ON, Canada, 2022).
- N. Moreno, D. Moreno-Chaparro, F. B. Usabiaga, and M. Ellero, “Hydrodynamics of spike proteins dictate a transport-affinity competition for SARS-CoV-2 and other enveloped viruses,” *Sci. Rep.* **12**, 11080 (2022).
- M. A. Kanso and A. J. Giacomin, “General rigid bead-rod macromolecular theory,” in *Recent Advances in Rheology: Theory, Biorheology, Suspension and Interfacial Rheology*, 1st ed., edited by D. De Kee and A. Ramachandran (AIP Publishing, Melville, NY, 2022), Chap. 2, pp. 2–1–2–32; Errata: Below Eq. (2.78), “...increases with N” should be “...increases with N^3 .” Above Eq. (2.80), “(77)” should be “(2.77).”
- M. A. Kanso, A. J. Giacomin, C. Saengow, and J. H. Piette, “Macromolecular architecture and complex viscosity,” *Phys. Fluids* **31**(8), 087107 (2019); Editor’s pick. Errata: In the caption of Fig. 1., “(rightmost)” should be “(leftmost),” and “(leftmost)” should be “(rightmost).”
- R. B. Bird, C. F. Curtiss, R. C. Armstrong, and O. Hassager, *Dynamics of Polymeric Liquids*, 2nd ed. (Wiley, New York, 1987), Vol. 2; Errata: In Table

- 16.4–1, under entry “length of rod” should be “bead center to center length of a rigid dumbbell.”
- ⁹R. B. Bird, O. Hassager, R. C. Armstrong, and C. F. Curtiss, Dynamics of Polymeric Liquids, 1st ed. (John Wiley and Sons Inc., New York, 1977), Vol. 2; Errata: In Problem 11.C.1 d., “and ϕ^2 ” should be “through ϕ^4 ”; in Eq. 13.6–17, “ R_{v1} ” should be “ R_{v2} .”
- ¹⁰P. Moscato, M. N. Haque, and A. Moscato, “Continued fractions and the Thomson problem” Research Square (published online 2022).
- ¹¹Y. Yang, D. G. Ivanov, and I. A. Kaltashov, “The challenge of structural heterogeneity in the native mass spectrometry studies of the SARS-CoV-2 spike protein interactions with its host cell-surface receptor,” *Anal. Bioanal. Chem.* **413**(29), 7205–7214 (2021).
- ¹²V. Chaurasia, Y.-C. Chen, and E. Fried, “Interacting charged elastic loops on a sphere,” *J. Mech. Phys. Solids* **134**, 103771 (2020).
- ¹³V. Chaurasia, “Variational formulation of charged curves constrained to a sphere,” Ph.D. thesis (Department of Mechanical Engineering, University of Houston, Houston, TX, 2018).
- ¹⁴L. M. Miller, L. F. Barnes, S. A. Raab, B. E. Draper, T. J. El-Baba, C. A. Lutomski, C. V. Robinson, D. E. Clemmer, and M. F. Jarrold, “Heterogeneity of glycan processing on trimeric SARS-CoV-2 spike protein revealed by charge detection mass spectrometry,” *J. Am. Chem. Soc.* **143**(10), 3959–3966 (2021).
- ¹⁵M. C. Pak, K.-I. Kim, M. A. Kalso, and A. J. Giacomin, “General rigid bead-rod theory with hydrodynamic interaction for polymer viscoelasticity,” *Phys. Fluids* **34**(2), 023106 (2022); Part 1.
- ¹⁶M. A. Kalso, M. C. Pak, K. Kwang-II, S. J. Coombs, and A. J. Giacomin, “Hydrodynamic interaction and complex viscosity of multi-bead rods,” *Phys. Fluids* **34**(4), 043102 (2022); Part 1, Editor’s Pick.
- ¹⁷M. C. Pak, R. Chakraborty, M. A. Kalso, K. Tontiwattanakul, K. Kwang-II, and A. J. Giacomin, “Coronavirus peplomer interaction,” *Phys. Fluids* **34**, 113109 (2022); Part 1, Editor’s Pick.
- ¹⁸Y. Xie, W. Guo, A. Lopez-Hernandez, S. Teng, and L. Li, “The pH effects on SARS-CoV and SARS-CoV-2 spike proteins in the process of binding to hACE2,” *Pathogens* **11**(2), 238 (2022).
- ¹⁹O. Hassager, “On the kinetic theory and rheology of multibead models for macromolecules,” Ph.D. thesis (Chemical Engineering Department, University of Wisconsin, Madison, WI, 1973).
- ²⁰O. Hassager, “Kinetic theory and rheology of bead–rod models for macromolecular solutions. II. Linear unsteady flow properties,” *J. Chem. Phys.* **60**(10), 4001–4008 (1974); Erratum: In Eq. (2), “1/2’ should be “–1/2” and “ \ll ” should be “ \gg .”
- ²¹W. E. Stewart and J. P. Sørensen, “Hydrodynamic interaction effects in rigid dumbbell suspensions. II. Computations for steady shear flow,” *Trans. Soc. Rheol.* **16**(1), 1–13 (1972).
- ²²J. H. Piette, L. M. Jbara, C. Saengow, and A. J. Giacomin, “Exact coefficients for rigid dumbbell suspensions for steady shear flow material function expansions,” *Phys. Fluids* **31**(2), 021212 (2019); Erratum: Above Eq. (83), “one other” should be “one other use.”
- ²³R. Chakraborty, D. Singhal, M. A. Kalso, and A. J. Giacomin, “Macromolecular complex viscosity from space-filling equilibrium structure,” *Phys. Fluids* **34**(9), 093109 (2022); Part 1.
- ²⁴M. A. Kalso, “Polymeric liquid behavior in oscillatory shear flow,” Master’s thesis (Polymers Research Group, Chemical Engineering Department, Queen’s University, Kingston, ON, Canada, 2019).
- ²⁵R. B. Bird and A. J. Giacomin, “Who conceived the complex viscosity?,” *Rheol. Acta* **51**(6), 481–486 (2012).
- ²⁶A. J. Giacomin and R. B. Bird, “Erratum: Official nomenclature of the society of rheology: $-\eta''$,” *J. Rheol.* **55**(4), 921–923 (2011).
- ²⁷J. D. Ferry, *Viscoelastic Properties of Polymers*, 3rd ed. (Wiley, New York, 1980).
- ²⁸R. B. Bird, R. C. Armstrong, and O. Hassager, Dynamics of Polymeric Liquids, 1st ed. (Wiley, New York, 1977), Vol. 1.
- ²⁹J. Guven and P. Vázquez-Montejo, “Confinement of semiflexible polymers,” *Phys. Rev. E* **85**(2), 026603 (2012).
- ³⁰J. Guven, D. M. Valencia, and P. Vázquez-Montejo, “Environmental bias and elastic curves on surfaces,” *J. Phys. A* **47**(35), 355201 (2014).
- ³¹I. B. Bischofs, S. S. Schmidt, and U. S. Schwarz, “Effect of adhesion geometry and rigidity on cellular force distributions,” *Phys. Rev. Lett.* **103**(4), 048101 (2009).
- ³²J. Thomson, “XXIV. On the structure of the atom: An investigation of the stability and periods of oscillation of a number of corpuscles arranged at equal intervals around the circumference of a circle; With application of the results to the theory of atomic structure,” *London, Edinburgh, Dublin Philos. Mag. J. Sci.* **7**(39), 237–265 (1904).
- ³³D. J. Wales and S. Ulker, “Structure and dynamics of spherical crystals characterized for the Thomson problem,” *Phys. Rev. B* **74**(21), 212101 (2006).
- ³⁴D. J. Wales, H. McKay, and E. L. Altschuler, “Defect motifs for spherical topologies,” *Phys. Rev. B* **79**(22), 224115 (2009).